

# A Fast and Sustainable Route to Bassanite Nanocrystals from Gypsum

Marcel Maslyk, Zsolt Dallos, Martha Koziol, Sebastian Seiffert, Tim Hieke, Katharina Petrović, Ute Kolb,\* Mihail Mondeshki,\* and Wolfgang Tremel\*

Calcium sulfate is an important construction material. More than 1600 million square meters of interior surfaces are covered with plasterboards in Europe each year. Plasterboard is manufactured by transforming mined or recycled gypsum ( $\text{CaSO}_4 \times 2 \text{H}_2\text{O}$ ) to bassanite ( $\text{CaSO}_4 \times \frac{1}{2}\text{H}_2\text{O}$ ) in a time- and energy-consuming heating process. A fast and sustainable way to produce bassanite by solvent-assisted milling, thereby eliminating the need for energy-intensive dehydration, is described. The milling reaction is complete after  $\approx 200$  min. Kinetic studies revealed that gypsum crystals transform to bassanite by shear forces during milling.  $^1\text{H}$  nuclear magnetic resonance (NMR) spectroscopic techniques and Fourier-transform infrared spectroscopy (FT-IR) show that the resulting bassanite nanocrystals are stabilized by surface functionalization with the auxiliary solvent methanol. Bassanite particles produced over extended milling times of 990 min form long-term stable dispersions without stabilizers and no signs of precipitation. Addition of water to bassanite leads to instant agglomeration, followed by a phase change to gypsum. The dispersibility in volatile methanol and the elucidation of the crystallization mechanism allow also for applications of the bassanite nanocrystals in hybrid materials.

and other products for the construction industry are based on this binder.<sup>[1]</sup> In addition, it is used as a component of cement,<sup>[2,3]</sup> for 3D printing,<sup>[4,5]</sup> as fertilizer or as food additive (cleaning of wines, refined sugar, canned vegetables and animal feed).<sup>[6]</sup> Its biocompatibility allows medical (e.g., plaster bandages, surgical and dental molds, production of toothpaste)<sup>[7–9]</sup> or pharmaceutical (drug delivery) use.<sup>[10]</sup>

When gypsum is heated above  $\approx 150$  °C in the dry state<sup>[11]</sup> (or at 75 °C in methanol–water solutions),<sup>[12]</sup> some of the crystal water is removed and  $\text{CaSO}_4 \times \frac{1}{2} \text{H}_2\text{O}$  (hemihydrate) is formed.<sup>[13]</sup> It is metastable at all temperatures and occurs in nature as the rare mineral bassanite<sup>[14]</sup> and as a biomineral in some deep-sea medusae.<sup>[15]</sup> Calcination of gypsum at higher temperatures ( $>800$  °C) yields anhydrite ( $\text{CaSO}_4$ ), which is the thermodynamically stable form at higher temperature, where all water of crystallization is removed.<sup>[16]</sup> The hydration of

anhydrite in water is kinetically hindered below 70 °C.<sup>[17,18]</sup> Therefore, anhydrite occurs in water-soluble mineral sediments that are formed by concentration/evaporation from aqueous solutions (evaporites).<sup>[19]</sup> Anhydrite and bassanite in soils are mainly formed by dehydration of gypsum. Bassanite–anhydrite successions away from the gypsum core show that bassanite is an intermediate in the transformation of gypsum to anhydrite.<sup>[20]</sup>


Calcium sulfate is one of the most abundant minerals on earth, and deposits were found even on Mars.<sup>[21]</sup> Huge deposits of gypsum and anhydrite occur in nature, and they are mined industrially.<sup>[22]</sup> Although industrially produced calcium sulfate is colloquially—but incorrectly—referred to as gypsum, it occurs in different hydration states with different physical properties. Chemically, the most common calcium sulfate phase is  $\text{CaSO}_4 \times \frac{1}{2}\text{H}_2\text{O}$  (hemihydrate), one of the world's most widely produced inorganic compounds (worldwide annual consumption  $\approx 150$  million metric tons).<sup>[13]</sup> Hemihydrate or the so-called plaster of Paris is produced by calcination of gypsum. With water it reacts back to gypsum in a rapid exothermic hydration process,<sup>[23]</sup> which accounts for the setting and hardening of plaster and cement materials. Therefore, biological systems generate hemihydrate far from chemical equilibrium.<sup>[24]</sup>

The steadily increasing demand for calcium sulfate has put the manufacturing and crystallization processes into the focus of investigations. There is increasing evidence that mineralization proceeds via multi-stage pathways including amorphous precursor

## 1. Introduction

Gypsum ( $\text{CaSO}_4 \times 2\text{H}_2\text{O}$ , dihydrate) has been used in construction since time immemorial. Today, stucco, screed, plasterboard, putty,

M. Maslyk, Z. Dallos, M. Koziol, S. Seiffert, T. Hieke, U. Kolb, M. Mondeshki, W. Tremel  
Department Chemie  
Johannes Gutenberg-Universität  
Duesbergweg 10-14, D-55099 Mainz, Germany  
E-mail: kolb@uni-mainz.de; mondeshki@uni-mainz.de; tremel@uni-mainz.de  
Z. Dallos, U. Kolb  
Department of Materials and Geoscience  
Technische Universität Darmstadt  
Petersenstrasse 23, 64287 Darmstadt, Germany  
K. Petrović  
Institut für Anorganische Chemie  
Gottfried Wilhelm Leibniz Universität  
Callinstrasse 3-9, D-30167 Hannover, Germany

 The ORCID identification number(s) for the author(s) of this article can be found under <https://doi.org/10.1002/adfm.202111852>.

© 2022 The Authors. Advanced Functional Materials published by Wiley-VCH GmbH. This is an open access article under the terms of the Creative Commons Attribution-NonCommercial-NoDerivs License, which permits use and distribution in any medium, provided the original work is properly cited, the use is non-commercial and no modifications or adaptations are made.

DOI: 10.1002/adfm.202111852

phases<sup>[25–37]</sup> and/or bassanite intermediates<sup>[25–31,33]</sup> that convert to gypsum via oriented attachment of nanocrystals.<sup>[28]</sup> Sub-3 nanometer particles have been identified by time-resolved small-angle X-ray scattering (SAXS) as primary species during crystallization,<sup>[32]</sup> and amorphous calcium sulfate, which can be stabilized by confinement,<sup>[38]</sup> has been shown to precede bassanite formation.<sup>[26,32]</sup> All calcium sulfate polymorphs can be prepared selectively by controlling the ratio of water/organic solvent mixtures.<sup>[30]</sup>

The industrial production of bassanite has high added value for a broad range of applications, most of which are based on the reversibility of the dehydration–rehydration reactions of gypsum. From an economic point of view, it is important to achieve dehydration in the shortest possible time with the lowest possible energy input, because raw material costs are very low and energy costs account for the lion's share of this calcination process.<sup>[39]</sup> The dehydration process is carried out successively during a period of time and depends on a variety of factors, especially the type of calcination, the granulation of the pure raw material, the amount of mineral impurities or other chemical compounds. Calcination temperatures between 100 and 200 °C are employed for the building industry. If dehydration is carried out in air furnaces and the energy is produced from fossil fuels, the ecological costs are particularly high. Using solar energy to produce bassanite by calcination of gypsum is one way to improve the carbon footprint.<sup>[40]</sup> Alternatively, bassanite can be obtained from gypsum via an autoclave process. In contrast to the large-scale production process of  $\beta$ -bassanite, the autoclave reaction favors the conversion of gypsum into  $\alpha$ -hemihydrate. This is promising in terms of its material properties and could find industrial applications.<sup>[41]</sup> To circumvent the high energy consumption and unfavorable continuous operation of the autoclave process, salt/acid or alcohol/water solution processes are pursued as alternative “green” approaches, but they are still operated often only at a laboratory or pilot scale.

We report on a new way to produce bassanite from gypsum by solvent-assisted grinding, which allows high energy conservation by bypassing calcination. Depending on grinding time and auxiliary solvent, even stable dispersions of bassanite can be produced. The great advantage of grinding is that scale-up is easily possible.<sup>[42]</sup> The transformation of gypsum into bassanite was tracked by Fourier transform infrared spectroscopy (FTIR), powder X-ray diffraction (PXRD), transmission (TEM) and scanning electron microscopy (SEM) to gain a mechanistic understanding of the transformation. The analysis revealed that bassanite formation proceeds via the reverse pathway to the formation of gypsum from bassanite in solution. <sup>1</sup>H nuclear magnetic resonance spectroscopy (<sup>1</sup>H NMR) and dynamic light scattering (DLS) showed that the stability of the CaSO<sub>4</sub> dispersions before and after drying was due to the facile exchange of crystal water against the auxiliary agent methanol. The good dispersibility of the product allowed the preparation of transparent films and thus may open new avenues for the preparation of CaSO<sub>4</sub>/polymer composites since both components can be blended in the organic co-solvent.

## 2. Results and Discussion

### 2.1. Ball-Milling Reaction

Solvent-assisted ball milling of gypsum was tested with cyclohexane and methanol. Full conversion to bassanite was

achieved with the polar auxiliary solvent methanol (ball-milled calcium sulfate, BMCS MeOH) as shown by FTIR, PXRD as well as TEM and SEM. With nonpolar cyclohexane, the conversion was incomplete (ball-milled calcium sulfate cyclohexane, BMCS-CH) (Figure 1 and Figure S1, Supporting Information).

Gypsum crystals have a plate-like morphology and diameters in the micrometer range (Figure 1C1,D1). Smaller platelets and nanocrystals with ill-defined morphologies are produced by ball milling in cyclohexane (Figure 1C2,D2). Needle-like nanocrystals were obtained in methanol (Figure 1C3,D3). Similar results have been reported for the precipitation of CaSO<sub>4</sub> from alcoholic solution.<sup>[31,43,44]</sup>

The kinetics of the grinding reaction was studied using “snapshots” after specific time intervals. Since the kinetics of the grinding reaction is slow, it could be stopped easily by quenching the hydration reaction with acetone. The quenched intermediates were investigated by FTIR spectroscopy and PXRD. The FTIR spectra show pronounced changes for the O–H stretching ( $\nu_1, \text{H}_2\text{O}$ ) and bending ( $\nu_2, \text{H}_2\text{O}$ ) modes of crystal water. A shoulder at 3604 cm<sup>-1</sup> in the  $\nu_1$  region indicates the formation of bassanite, in harmony with the X-ray diffractograms where the 200, 400 and 134 reflections of bassanite appeared after 30 minutes of milling (Figure 1B,D). The intensity of the O–H stretching modes ( $\nu_3$  3509 cm<sup>-1</sup>,  $\nu_1$  3399 cm<sup>-1</sup>) of gypsum decreased, whereas the intensity of the O–H stretches ( $\nu_3$  3604 cm<sup>-1</sup>,  $\nu_1$  3552 cm<sup>-1</sup>) of bassanite increased. A broad intensity distribution remained between 3500 and 2900 cm<sup>-1</sup> (Figure 2A,C) compatible with disordered O–H groups due to the occlusion of methanol. The X-ray diffractograms showed a decreasing intensity and a broadening of the 020 and 021 reflections with time due to the decreasing particle size. After  $\approx$ 30 min of milling the first reflections of bassanite appeared, which broadened slightly after prolonged milling. Only traces of gypsum remained after  $\approx$ 100 min and pure bassanite was formed after  $\approx$ 200 min. Vibrational spectroscopy can detect local order in the semi-crystalline or even amorphous state. In the IR spectra, the intensities of the vibrational bands of gypsum decreased after 100 min, but they were still clearly visible.

The phase gypsum to bassanite transformation was complete after about 3 h (i.e., 200 min). Extending the milling time further only led to a decrease in particle size and eventually after 990 min to the formation of a stable dispersion of bassanite nanoparticles.

TEM images show the formation of needle-like nanocrystals with diameters of a few nm and lengths of  $\approx$ 100 nm (Figure 1C). Different from TEM, which provides static information concerning the structure and aggregation of dry samples, DLS is an ensemble technique that reveals the dynamic behavior of nanocrystals in dispersion (Figure 3A,B). DLS revealed the presence of polydisperse bassanite nanorods with hydrodynamic radii of  $R_{\text{H},1} = 165$  nm,  $R_{\text{H},2} = 729$  nm, and  $R_{\text{H},3} = 3.9$   $\mu\text{m}$  in methanolic dispersion (Figure 3A).

### 2.2. Solvent Surface Effect

The dispersion of bassanite nanorods obtained by extended grinding in methanol (990 min) was very stable and showed an excellent miscibility with organic solvents like ethylene glycol (Figure S2, Supporting Information) The molecular interactions

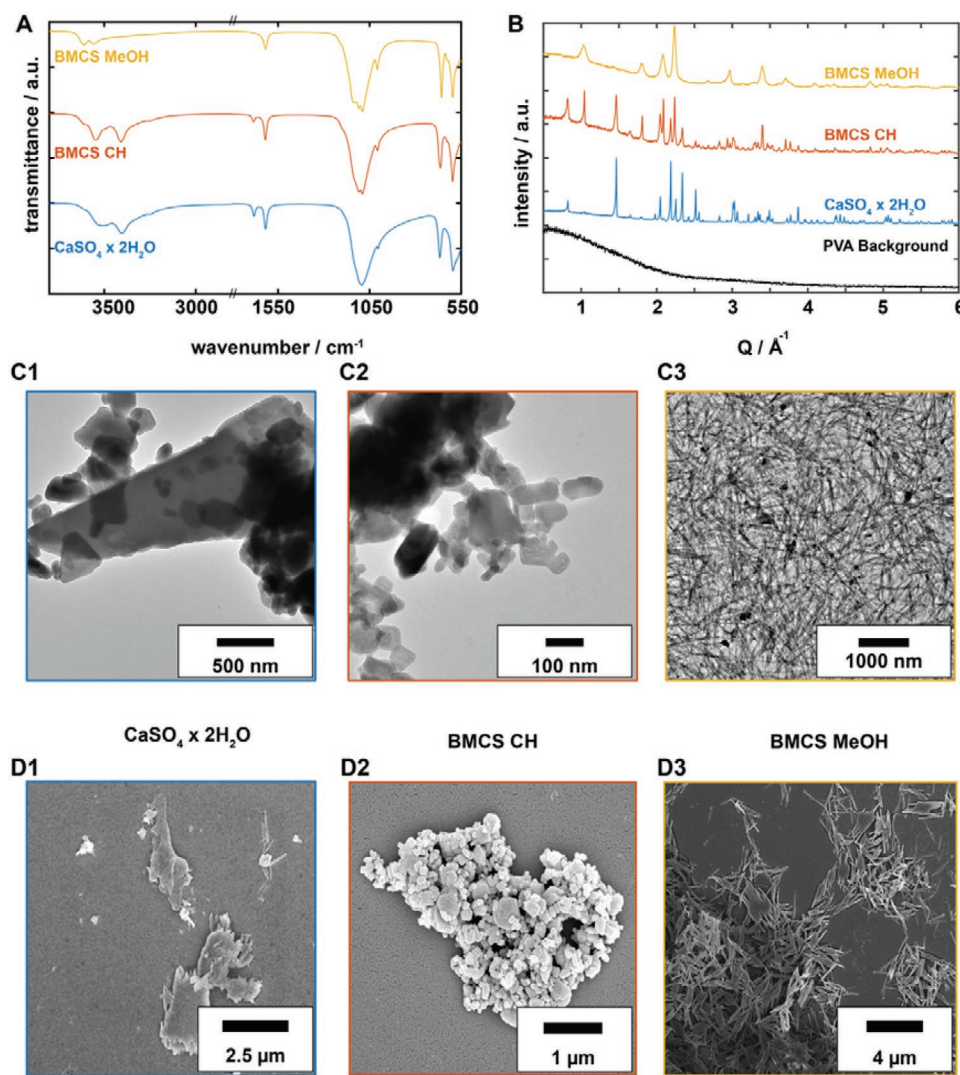


**Figure 1.** A) Overview FTIR spectra, B) X-ray diffractograms, C) TEM and D) SEM images of pure gypsum ( $\text{CaSO}_4 \times 2\text{H}_2\text{O}$ , blue lines and squares), gypsum ball-milled with cyclohexane (mixture of  $\text{CaSO}_4 \times 2\text{H}_2\text{O}$  and  $\text{CaSO}_4 \times 0.5\text{H}_2\text{O}$ , red lines and squares) and gypsum ball-milled in methanol ( $\text{CaSO}_4 \times 0.5\text{H}_2\text{O}$ , yellow lines and squares).

responsible for the stability of the dispersion were elucidated by  $^1\text{H}$  liquid and solid-state NMR spectroscopy.

To gain resolution due to the fast molecular motion resulting in averaging out of the anisotropic interactions (anisotropy of the chemical shift, dipole–dipole couplings and quadrupole couplings)  $^1\text{H}$  solution NMR methods were used to further investigate the bassanite nanoparticles.

The  $^1\text{H}$  ssNMR spectrum of milled gypsum after centrifugation and subsequent drying of the dispersion was compared with that of gypsum (as starting material in the mechanochemical reaction) (Figure 4A). The  $^1\text{H}$  resonance in the spectrum of gypsum milled in methanol (BMCS MeOH) was significantly broadened, whereas the  $^1\text{H}$  ssNMR spectrum of non-milled gypsum recorded at 10 kHz MAS showed a signal at 4.60 ppm with a full width at half-maximum (fwhm) of 1700 Hz, which is attributed to the structural water. The spectrum after deconvolution consists of three signals located at 1.3 ppm (fwhm 2110 Hz), 4.4 ppm (790 Hz) and 4.8 ppm

(2670 Hz), which could be assigned to methyl protons as well as two different hydroxyl protons, respectively. The broader and more intense hydroxyl resonance is related to structural water in bassanite (presumably different polymorphs of bassanite with respect to the water content). The broadening of the resonances of methanol molecules at the surface is due to their lower dynamics owing to stronger dipolar proton–proton couplings which cannot be averaged out by magic angle spinning at moderate spinning frequencies.

The  $^1\text{H}$  NMR spectrum of bassanite nanoparticles in methanol showed four signals. Two of them (3.2 and 4.7 ppm, Figure 4B) correspond to the  $\text{CH}_3$  and OH resonances of methanol (Figure S3, Supporting Information). The other two resonances at 4.4 ppm (Figure 4B, signals marked by\*) are assigned to water incorporated in the bassanite structure. However, they might originate as well from solvent molecules functionalizing the nanoparticle surface in the slow exchange regime. Temperature dependent  $^1\text{H}$  NMR spectra were recorded, to enhance

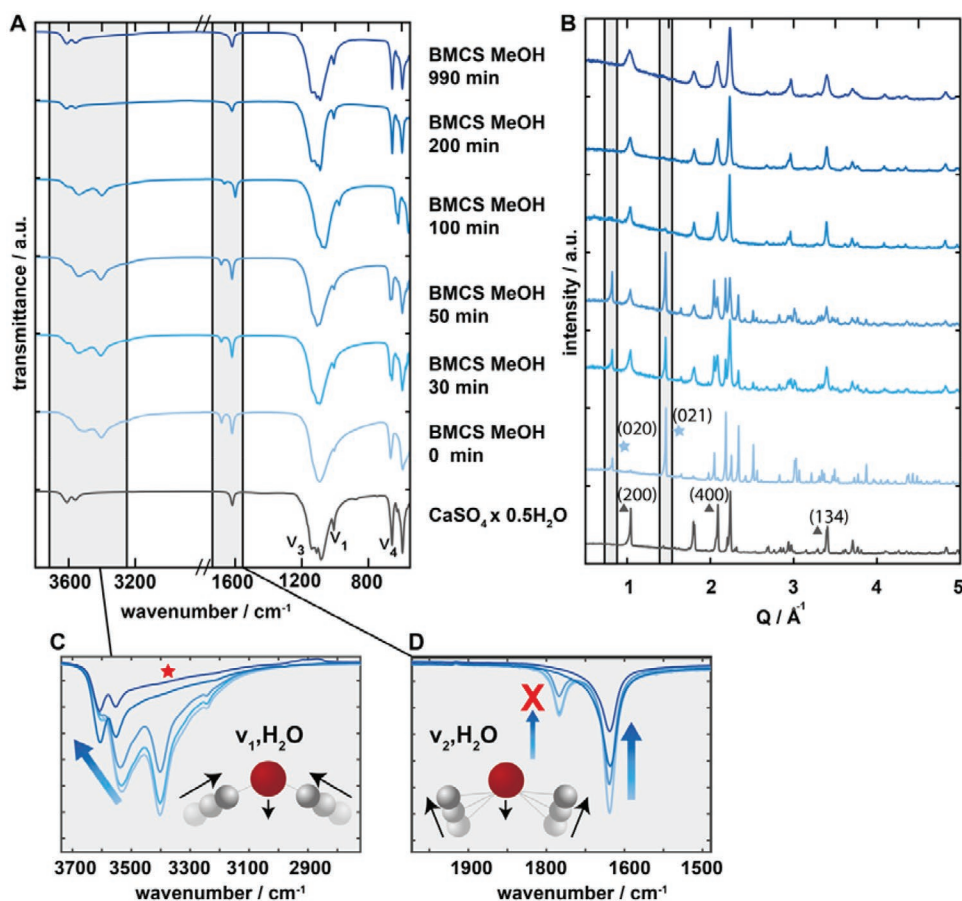


**Figure 2.** Progression of the milling reaction after different reaction times, monitored by A) FTIR spectroscopy and B) PXRD. Reflections of bassanite are marked with triangles, reflections of gypsum with stars. The reaction time is coded by the blue color depth. Insets (C, D) show magnified FTIR spectra of the O-H stretching and bending modes.

the exchange and changes in the chemical shifts of the solvent hydroxyl group and the signals at 4.4 ppm until they coalesced (in the fast exchange regime). These experiments did not reveal a coalescence of the signals at 4.4 and 4.7 ppm. The signals at 4.4 ppm coalesce at higher temperatures due to faster particle

motion (Figure S4, Supporting Information). This observation may be explained by an exchange of water molecules. Thus, we exclude the possibility of the resonance at 4.4 ppm to arise from surface functionalizing solvent hydroxyl groups and attribute it to two different water environments in the bassanite structure.

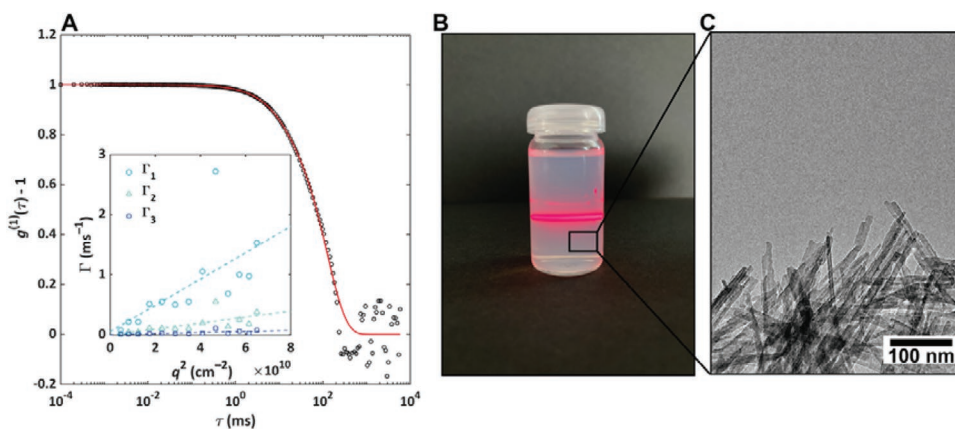


**Figure 3.** A) Normalized field correlation function  $g^{(1)}(\tau)$  of the nanoparticle dispersion in methanol (black open circles) and fit to a tri-exponential decay (red line). Inset:  $\Gamma_{1-3}$  versus  $q^2$  reveals at least three diffusing species. B) Tyndall scattering of a laser beam by bassanite nanoneedles in methanol dispersion. C) TEM image showing bassanite nanoneedles with lengths of  $\approx 100$  nm.

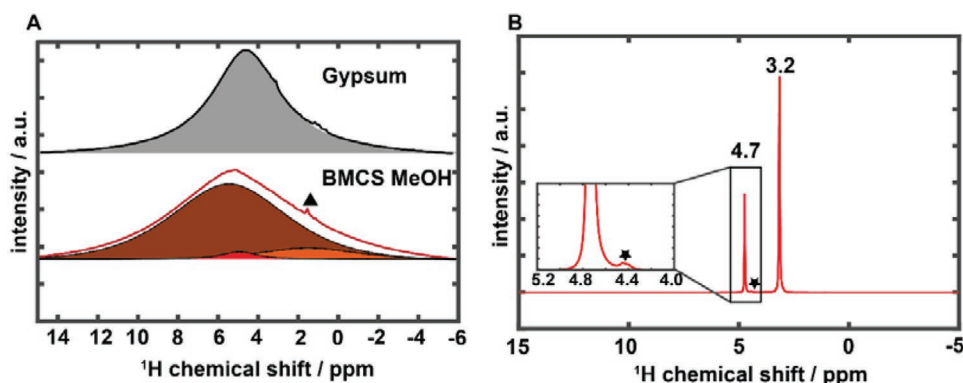


**Figure 4.** A) Comparison of the  $^1\text{H}$  solid state NMR spectrum of gypsum and BMCS MeOH showing a broadened signal in BMCS MeOH. B)  $^1\text{H}$  NMR spectrum of the bassanite dispersion in methanol.

The  $\text{CaSO}_4 \times 0.5 \text{H}_2\text{O}$  nanoparticles were further investigated by  $^1\text{H}$  NOESY NMR spectroscopy. This NMR experiment probes the through space proton dipole-dipole couplings revealing contacts between dipolar coupled proton species in close proximity, i.e., 4–5 Å, as off-diagonal peaks. The  $^1\text{H}$  NOESY NMR spectrum recorded with a mixing time of 1 ms (Figure 5A) reveals one broad diagonal and two off-diagonal signals (Figure 5B). The broad diagonal signal ranging from 4.3 to 5.1 ppm for the OH protons of methanol is related to a distribution of environments and is assumed to arise from the interaction of the hydroxyl protons with different bassanite surface sites. The two off-diagonal signals ((4.5 ppm, 4.8 ppm) and (4.4 ppm, 4.7 ppm)) are related to the water protons confined in the hexagonal channels in the crystalline structure of bassanite in close proximity to the nanoparticle surface and thus methanolic hydroxyl groups. To confirm this assumption diffusion-based NMR experiments were recorded for pure methanol (Figure 5C, red lines) and the bassanite dispersion (Figure 5C, black lines) and subsequently overlaid. On one hand, the methanol in the dispersion would diffuse more slowly compared to the pure solvent due to exchange with the surface-bound methanol. On the other hand, an equivalent diffusion coefficient for the water in the bassanite structure and the surface methanol molecules are expected as the particle movement would be the rate determining step. Indeed, the recorded spectra (Figure 5C) show a difference between the  $D$  values for pure methanol ( $7.9 \times 10^{-9}$ ) and that in the bassanite dispersion ( $1.2 \times 10^{-9}$ ). The observed difference in the diffusion coefficients confirms the functionalization of the nanoparticles by surface-bound methanol molecules, which most likely exchange with the surrounding solvent molecules. This is the reason for the stability of the dispersion in methanol and other polar solvents. The interaction of methanol with bassanite surfaces results in a slower overall diffusion because the solvation shell also contributes to the hydrodynamic radius of the bassanite particles. DOSY experiments (Figure 5D) show that the signals at 4.4 ppm have the same diffusion coefficient as some of the methanol molecules. This confirms the presence of water in the bassanite structure. Incorporation of methanol in the bassanite pores during the synthesis of the nanoparticles was not confirmed but cannot be ruled out.

In conclusion, methanol functionalizes the bassanite nanoparticle surfaces thereby stabilizing the nanoparticle dispersion in polar organic solvents. The surface functionalization is confirmed

by the fact that the ligands have the same diffusion coefficient as the water molecules incorporated in the bassanite structure. Two different off-diagonal resonance signals in the NOESY spectrum may arise from different types of bassanite polymorphs due to differences in the hydration state of bassanite. Milling in methanol may lead to the formation of sub-hydrates in the calcium sulfate system or to a partial substitution of water by methanol.

### 2.3. Thermal Stability and Microstructure

Thermal analysis allows to analyze physical changes with time and temperature when bassanite nanocrystals are heated or cooled. The TGA/TGA profile of the bassanite nanocrystals air-dried from dispersion shows an endothermic mass loss of  $\approx 7.9\%$  at  $\approx 140^\circ\text{C}$  (Figure 6A). The transition of  $\text{CaSO}_4 \times \frac{1}{2} \text{H}_2\text{O} \rightarrow \text{CaSO}_4$  corresponds to a mass loss of  $6.3\%_w$  for crystal water. Partial substitution of water by methanol leads to the observed higher mass loss. Based on the analytical information from  $^1\text{H}$  MAS-NMR that  $\approx 20\%$  of the crystal water is replaced by methanol (corresponding to a composition  $\text{CaSO}_4 \times 0.4 \text{H}_2\text{O} \times 0.1 \text{CH}_3\text{OH}$ ) a mass loss of  $7.1\%$  is expected for a  $\text{H}_2\text{O}/\text{CH}_3\text{OH}$  ratio of 4/1, close to the experimental value. PXRD and Rietveld analysis of the product obtained by milling gypsum in methanol showed the formation of bassanite with cell parameters of  $a = 12.083 \text{ \AA}$ ,  $b = 6.903 \text{ \AA}$  and  $c = 12.683 \text{ \AA}$  and a crystallite size of  $\approx 30 \text{ nm}$  (Figure 6B).

This result seems to contradict the broad distribution obtained with DLS and conventional TEM imaging. However, one must consider that the particle size distribution in a solid bulk sample corresponds only to a limited extent to a model of discrete spherical particles in dispersion (DLS) or individual particles in electron microscopy (TEM). When gypsum was ball-milled in cyclohexane, two DTA signals at 110 and  $150^\circ\text{C}$  with a mass loss of 15% were obtained. Since a mass loss of 20% is expected for pure gypsum, this is compatible with a partial (80%) conversion of gypsum to bassanite (Figure S5, Supporting Information).

Figure 6C1 shows the TEM image of a single bassanite needle with a length of  $\approx 500 \text{ nm}$ . A magnified view (Figure 6C2) shows a periodic arrangement of lattice planes in the nanocrystal. The fast-Fourier transform (FFT) was calculated with the Gatan Digital Micrograph Software<sup>[45]</sup> (Figure 6C3), and the FFT image

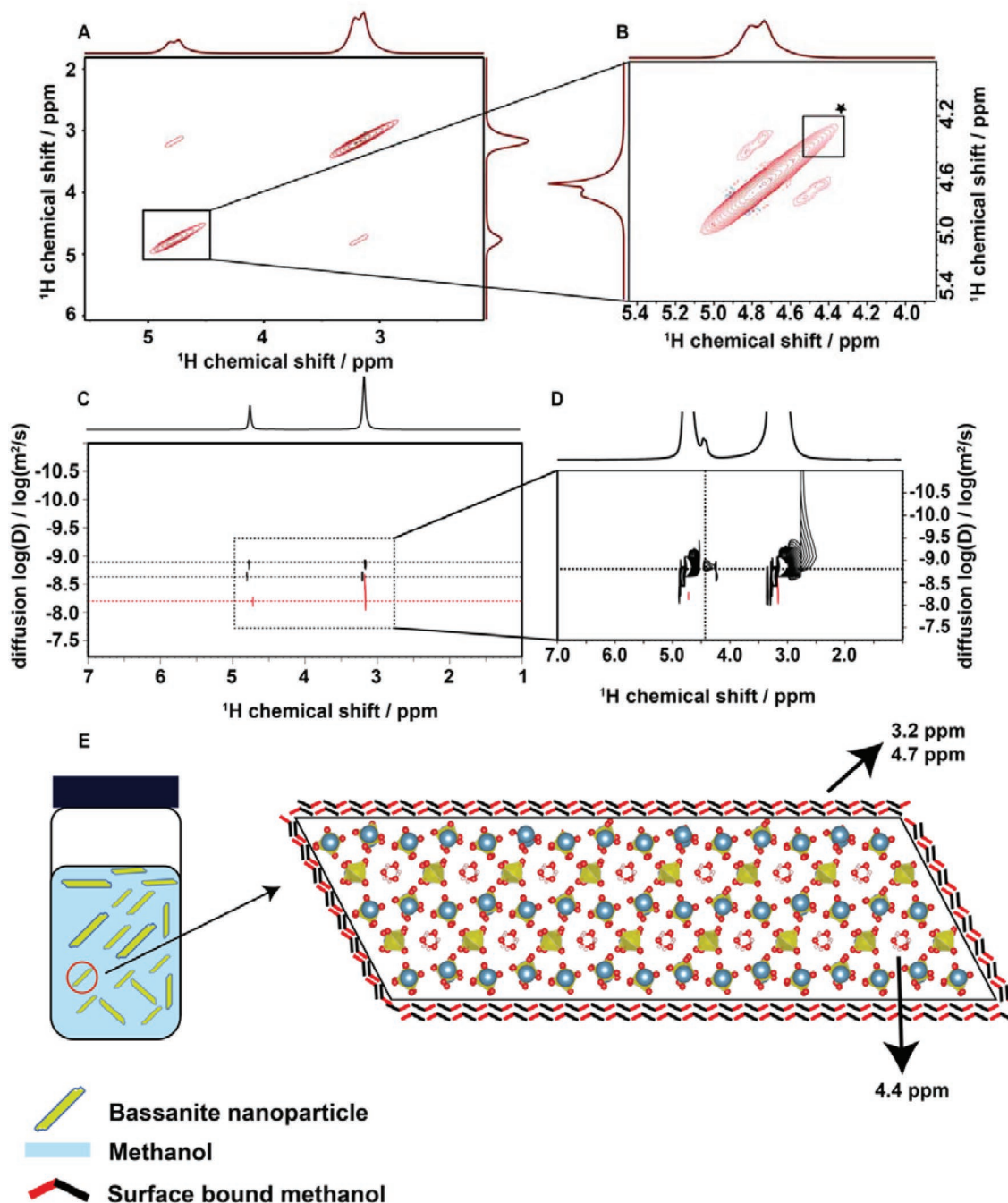


**Figure 5.** A)  $^1\text{H}$  NOESY NMR spectrum depicting a coupling between the O–H groups of methanol molecules resonating at 4.8 ppm. B) Magnification of the inset in the  $^1\text{H}$  NOESY NMR spectrum revealing coupling of the water signal of bassanite at 4.4 ppm with methanol molecules. C)  $^1\text{H}$  DOSY spectra of methanol (red) and bassanite dispersion (black). The slower diffusion of methanol molecules in bassanite dispersions indicates a stabilization by surface-bound methanol. D) Magnification of the inset in the  $^1\text{H}$  DOSY spectrum of methanol (red) and bassanite dispersion (black), revealing the diffusion coefficient of bassanite. E) Surface functionalization of a bassanite nanoparticle by weakly bound methanol molecules. The projection along [001] shows the distinct hexagonal channels filled with water molecules.

was indexed based on the bassanite structure (Figure 6B). Since the lattice planes were not compatible with a specific zone the needle must consist of several crystalline domains, forming a single needle by oriented attachment.<sup>[28]</sup> An inverse Fourier transform of the calculated FFT shows dislocations and contrast changes compatible with a non-uniform  $d$  spacing.

Although PXRD and HRTEM show the samples to consist mainly of bassanite, small amounts of anhydrite were found in HRTEM, indicating that mechanochemical dehydration is feasible by adjusting the milling conditions. Milling of commercial bassanite in methanol and cyclohexane showed indeed the formation of anhydrite (Figure S6, Supporting Information).

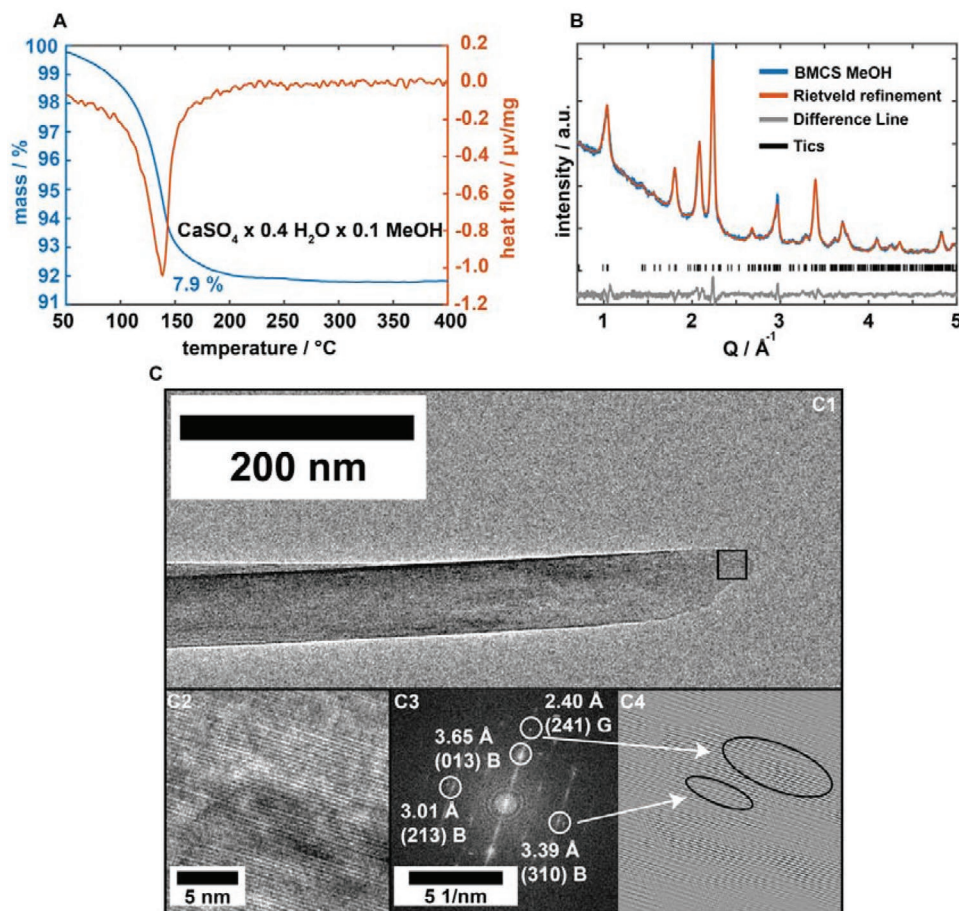


**Figure 6.** A) TGA (blue line) and DTA traces (red line) for dried bassanite nanocrystals and B) Rietveld refinement. C) TEM image (C1) and HRTEM image (C2) of the dried bassanite nanocrystals showing the lattice planes, the reduced fast-Fourier transformation (FFT) (C3) and inverse-transformed Fourier transformation (IFFT) (C4).

#### 2.4. Gypsum to Bassanite Transformation

TEM and SEM “snapshots” were taken at different stages of the milling and crystallization process. For this purpose, the reaction was stopped, aliquots were taken, centrifuged and washed with acetone to prevent further phase transformations. The corresponding samples were then dispersed in acetone and dropped onto a TEM grid or SEM holder respectively.

Micrometer-sized platelets were present in the TEM and SEM at the start of the grinding reaction (Figure 7A1,B1). PXRD showed that bassanite was formed after a short reaction time. Crystallites with needle-like and plate-like morphologies were present in TEM and SEM (Figure 7A2, B2, 30 min). This indicates that the platelets are broken up by shear forces and separated from each other by surface functionalization with methanol. The crystal structure of gypsum is composed of layers of tightly bound  $\text{Ca}^{2+}$  and  $\text{SO}_4^{2-}$  ions, separated by water molecules stabilized by a network of hydrogen bonds. We assume that shear forces from the milling process cleave gypsum crystals parallel to the (010) plane (Figure 7C1). Due to its high polarity, methanol might adsorb to these surfaces and substitute surface-bound water molecules thereby weakening the hydrogen-bonded network. In addition, it plays a fundamental role in

stabilizing the bassanite nanoparticles (Figure 7C2). The heat generated by the collisions can lead to partial dehydration (i.e., desorption of hydrate-water), where the resulting vacancies on the surfaces are filled with methanol. The  $\text{Ca}^{2+}/\text{SO}_4^{2-}$  blocks occurring in the different  $\text{CaSO}_4$  polymorphs make a structural rearrangement feasible. A shift in the layers along [010] and [001] leads to the formation of hexagonal channels, similar to those occurring in the bassanite structure. (Figure 7D1–D3)

Other than in methanol, grinding in cyclohexane does not lead to the formation of specific morphologies and the transformation to bassanite was incomplete (Figure S7, Supporting Information). PXRD and FTIR analysis show that gypsum transformed to bassanite completely with increasing grinding time ( $\approx 200$  min). The corresponding TEM and SEM images show needle-like crystallites after 200 min (Figure 7A3,B3). A stable dispersion was obtained for still higher reaction times ( $\approx 990$  min), and the needles had a different aspect ratio (Figure 7A4,B4). The needles were not stable in the electron beam. Rapid imaging was required to prevent radiation-induced dehydration (Figure S8, Supporting Information). Their formation can be explained by a stepwise reduction in particle size with concomitant stabilization by surface binding of the auxiliary agent methanol. TEM and SEM analysis show that the bassanite nanocrystals assemble into needle-like crystallites.

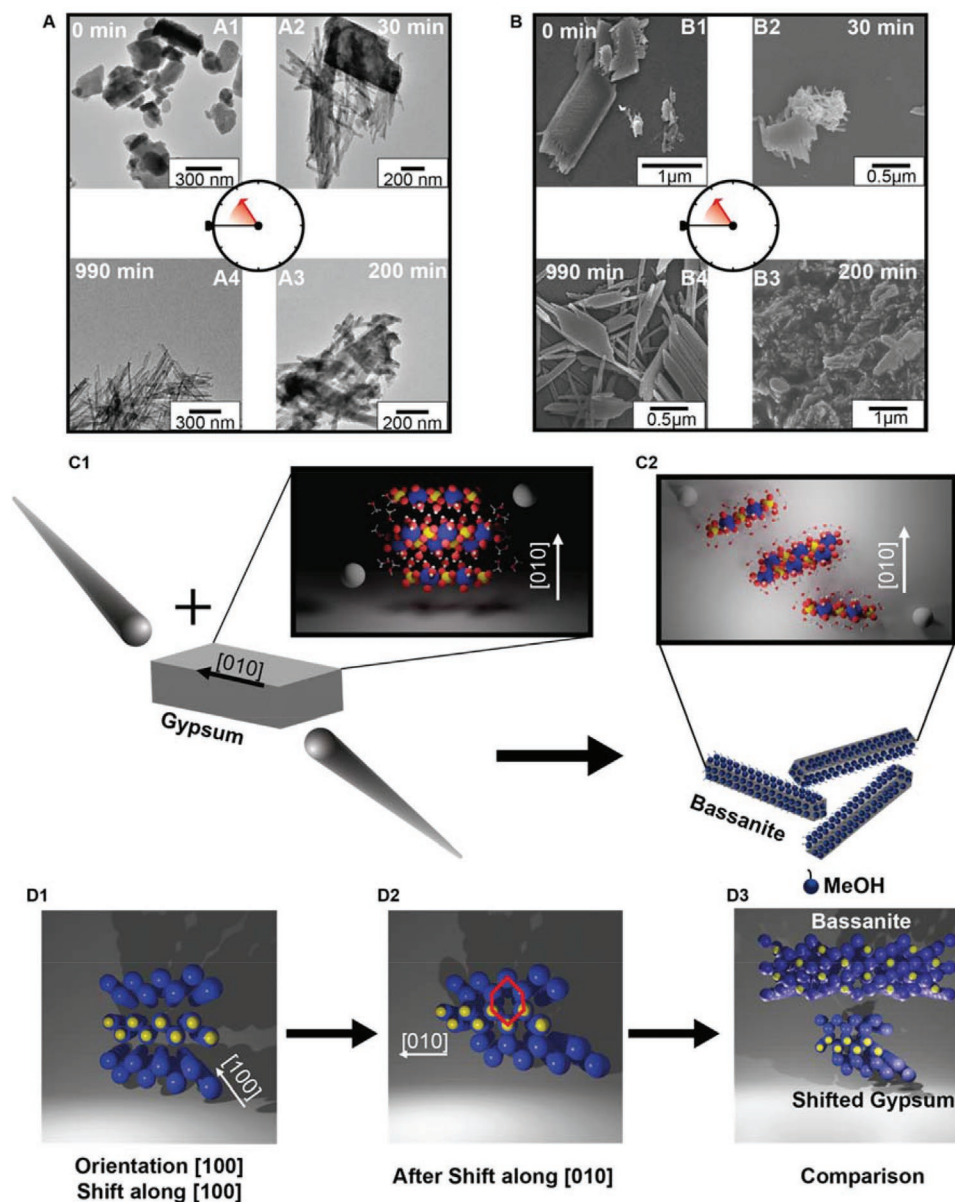


**Figure 7.** A) TEM and B) SEM images taken after 0, 30 220 and 990 min of milling showing the transformation of plate like structures into fine needles. C1) Schematic sketch of the effect of methanol assisted ball milling. C2) Sketch of functionalized bassanite nanoparticles, resulting from a cleavage parallel to (001). D1) View of calcium and sulfur atoms shifted along [100]. D2) A shear force parallel to [010] may lead to the formation of hexagonal channels (red hexagon). D3) Comparison of the gypsum and bassanite structures along the channels.

## 2.5. Film Casting

Bassanite nanocrystals prepared by ball-milling form clear and stable dispersions in methanol (Figure 8A, inset). These dispersions are miscible with a variety of organic solvents (e.g., acetone, different alcohols and ethylene glycol) without any signs of precipitation. This allowed to cast dense nanoparticle films on a glass slide, which form transparent films after drying (Figure 8A). Mixing the dispersion with non-polar solvents such as cyclohexane lead phase separation. Adding a few drops of water to the dispersion causes an immediate precipitation of needle-like gypsum nanocrystals ( $\approx 20 \mu\text{m}$  in length, Figure 8C1, inset).

The stability of the clear dispersions obtained after extended milling allowed to cast dense films on glass slides, which form transparent coatings after drying. This might lead to interesting applications in sensors based on hydration reactions.<sup>[46]</sup> To assess the feasibility of this approach, a glass slide was dip-coated with the dispersion and examined by laser microscopy after drying (Figure 8A). A transparent coating was formed without any perceptible change in the refractive behavior, as shown by the zoomed image sections in the red/blue boxes. Micro-sized crystal agglomerates were formed upon contact with water due to the rapid exchange of methanol surface ligands by water, i.e., water leads to rehydration of the methanol-stabilized bassanite nanocrystals and the ensuing formation of gypsum.



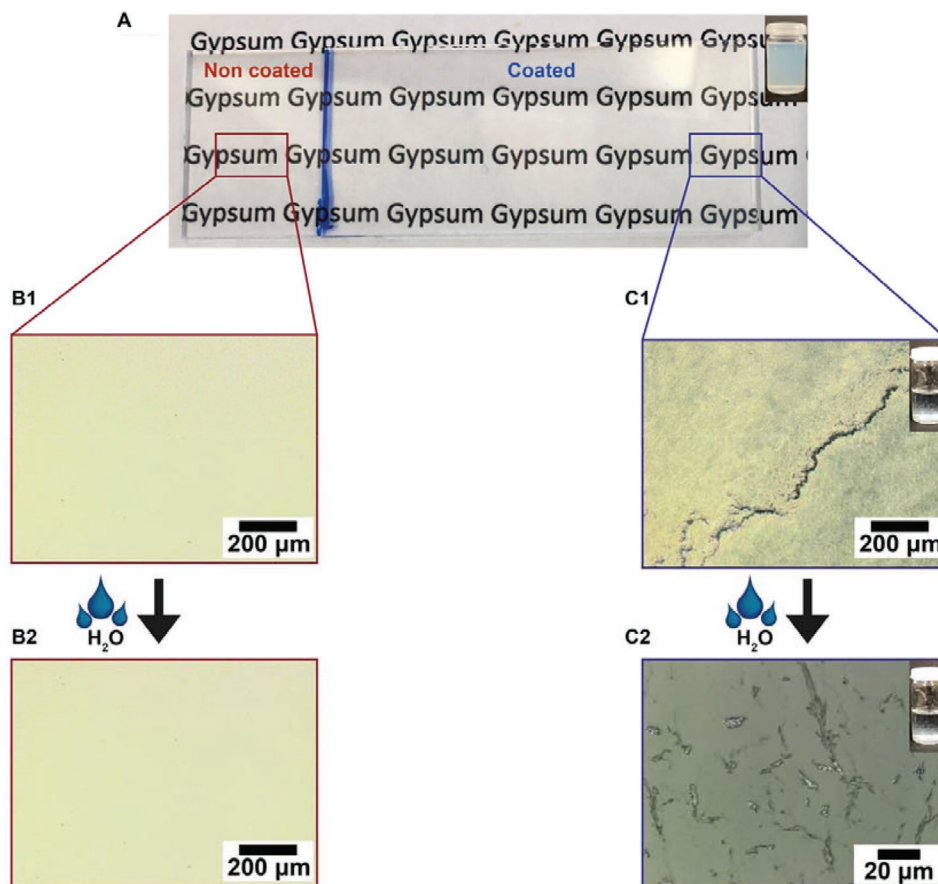


**Figure 8.** A) Laser microscopy image of a dense bassanite film on a glass slide, fabricated from a clear and stable dispersion in methanol (inset). The zoomed image sections (B1, C1) in the red and blue boxes show laser microscopy images of the corresponding areas on the glass slide. Adding a few drops of water led to immediate precipitation in the dispersion (insets C1 and C2). The non-coated part of the glass slide shows no changes (B2) after adding water, whereas gypsum crystals form on the coated part (C2).

### 3. Conclusion

We developed a new energy-saving and sustainable synthesis for bassanite nanoparticles by solvent-assisted ball milling of gypsum. The milling reaction is complete after only 3 h. The kinetics and the mechanism of the milling reaction were elucidated by making “snapshots” of the reaction by stopping the milling after different time intervals. During milling, gypsum platelets transform to bassanite needles by shear forces. The bassanite nanocrystals are polydisperse with a size ranging from 20 nm to several hundred nm and they are separated and stabilized by surface complexation with methanol, the dispersing agent. <sup>1</sup>H NMR and FTIR spectroscopy revealed that surface-bound methanol “passivates” the bassanite particles with needle-like morphology, thereby preventing aggregation and precipitation. Bassanite nanoparticles prepared by extended ball milling form long-term stable dispersions in methanol with no additional stabilizers and no evidence of precipitation. Methanol is easily recovered because of its low boiling point. Adding water to bassanite dispersions in methanol leads to instant agglomeration, followed by a phase transition to gypsum. The dispersibility in the volatile organic solvent methanol and the elucidation of the crystallization

mechanism allow for applications of the bassanite nanocrystals in hybrid materials, e.g., for transparent optical films or as disposable humidity sensors.

The most important advance is that plasterboards from gypsum might be made more efficiently in the future. Every year in Europe, more than 1.5 billion m<sup>2</sup> of the interior surface is covered with plasterboards,<sup>[47]</sup> which are used for partition walls and the cladding of walls, ceilings, roofs or floors, or decorative plaster. To produce plasterboard, manufacturers typically dehydrate the mined gypsum into bassanite in a very time- and energy-consuming heating process. Our study describes a simple and sustainable way to produce bassanite in a short milling process, thereby eliminating the need for energy-intensive dehydration. Since grinding is a standard process in the construction industry, large-scale implementation seems feasible. Based on the specific properties of a standard ball mill in a research laboratory (with a capacity of ≈10 g), we estimate an energy consumption of about 10 GJ per ton of bassanite, while the specific thermal energy consumption for stucco is given as 1 GJ per ton.<sup>[48]</sup> Although the energy consumption for milling appears to be higher at first glance, it should be borne in mind that this calculation is based on a simple multiplication on a scale of one-to-one, without any optimization of the

parameters being taken into account. Even the use of containers holding one hundred times the quantity (1 kg) would result in the estimated energy consumption being only one tenth of the energy consumption required at present.

## 4. Experimental Section

**Materials:** Calcium sulfate dihydrate (Sigma-Aldrich), acetone (99.5%, puriss. p.a., Riedel-de Haën), methanol (HPLC grade, Fisher Chemicals), cyclohexane (analytical reagent grade, Fisher Chemicals,) and doubly-deionized water (resistivity > 18 mΩ cm).

**Synthesis of BMCS MeOH:** 500 mg of calcium sulfate dihydrate (3.6 mmol) was treated with methanol (9 ml) in a planetary ball mill (pulverisette 7 Classic, Fritsch). The starting materials were transferred together with 7.5 grams of grinding balls (about 2000 balls, 1 mm diameter, ZrO<sub>2</sub>) into ZrO<sub>2</sub> grinding jars. The mixture was milled for different time intervals. To avoid overheating 10 min of grinding and a subsequent 10 min rest phase were used. Therefore, 200 min of milling corresponds to a reaction time of 400 min. Afterwards, decantation and subsequent washing by methanol was used to separate the product and ZrO<sub>2</sub> balls.

**Synthesis of BMCS CH:** 500 mg of calcium sulfate dihydrate (3.6 mmol) was treated with cyclohexane (9 ml) in a planetary ball mill (pulverisette 7 Classic, Fritsch). The starting materials were transferred together with 7.5 grams of grinding balls (about 2000 balls, 1 mm diameter, ZrO<sub>2</sub>) into ZrO<sub>2</sub> grinding jars. The mixture was milled for different time intervals. To avoid overheating 10 min of grinding and a subsequent 10 min rest phase were used. Therefore 200 min of milling corresponds to a reaction time of 400 min. Afterwards, decantation and subsequent washing by methanol was used to separate product and ZrO<sub>2</sub> balls.

**Film Fabrication:** Transparent calcium sulfate films were prepared by depositing the nanoparticle dispersion on a glass slide and quickly evaporating the solvent in a drying chamber at 80 °C.

**Characterization:** Samples for transmission electron microscopy were prepared by drop-casting 20 μL of the respective sample dispersion on 400 mesh carbon copper grids (Plano GmbH, Wetzlar, Germany). The samples were measured with a FEI Tecnai Spirit TWIN LaB<sub>6</sub> at 120 kV equipped with a Gatan US1000 CCD-camera (2048 × 2048 pixels) and a FEI Tecnai F30 S-TWIN at 300 kV equipped with a Gatan US4000 CCD-camera (4096 × 4096 pixels). A 70 μm condenser aperture and standard illumination settings were used for the TEM images acquisition. The high-resolution TEM (HRTEM) images were recorded at a primary magnification of 590 000. The images were hardware-binned by 2 resulting 2k × 2k images with a physical pixel size of 0.41 Å. For data processing Digital Micrograph software was used.

Dusk-free acetone-rinsed quartz glass cuvettes were filled with pre-filtered (syringe filter Millex AA, pore size: 800 nm, diameter: 25 mm) dispersion solutions. All light scattering experiments were performed on a multi-goniometer ALV-CGS-8F SLS/DLS 5022F, equipped with a Uniphase He/Ne laser (25 mW, 632.8 nm) and an ALV-7004 multi-τ correlator connected to an ALV/high QE APD avalanche photodiode in pseudo-cross-correlation mode (ALV-Laser Vertriebsgesellschaft mbH, Langen, Germany). Temperature control (±0.1°C) during measurements is assured by a Lauda ultrathermostat RKS C6 (Lauda Dr. Wobser GmbH, Lauda, Königshofen, Germany). The experiments and data acquisition were controlled by an ALV software correlator ALV500/E/EPP-ALV-60x0-WIN 3.0.3.15. Angular dependent measurements were performed in the range of 30° < θ < 150° corresponding to wave vectors of  $q = (4\pi n \sin(\theta/2))/\lambda$  with the scattering angle θ, the wavelength λ, and the refractive index  $n = 1.3288$  (for methanol at 20 °C). The recorded intensity correlation functions  $g^{(2)}(q, \tau)$  were converted via Siegert relation  $g^{(2)}(\tau) - 1 = \beta + |g^{(1)}(\tau)|^2$  into the field correlation function  $g^{(1)}(\tau)$  with the specific instrument factor β. For polydisperse solutions with diffusing particles of a multitude of sizes, the overall intensity decay resembles a superposition of several exponential decays. Due to a broad sample polydispersity, the recorded amplitude correlation functions  $g^{(1)}(\tau)$  were fitted to a tri-exponential decay function of the form  $g^{(1)}(q, \tau) = A + B \cdot \exp(-\Gamma_1 \tau) + C \cdot \exp(-\Gamma_2 \tau) + E \cdot (-\Gamma_3 \tau)$  with the

decay rates  $\Gamma_n = D_n q^2$ , the offset A, and the amplitudes B, C, and E. The diffusion coefficients  $D_n$  were converted into hydrodynamic radii using the Stokes–Einstein equation  $R_{H,n} = \frac{k_B T}{6\pi\eta D_n}$  with the Boltzmann constant  $k_B$ , the temperature T, and the solvent dynamic viscosity η.

ATR-IR spectroscopy was performed at a Nicolet iS10 Spectrometer manufactured by Thermo Scientific. The spectra were recorded in a range from 650 to 4000 cm<sup>-1</sup> with a resolution of 1.4 cm<sup>-1</sup> per data point.

The <sup>1</sup>H spectra were recorded on a Bruker Advance 400 DSX NMR spectrometer at a <sup>1</sup>H frequency of 399.87 MHz. A commercial 3 channel 4 mm Bruker probe head at 10 kHz magic angle spinning (MAS) averaging 32 scans was used. The spectra were referenced to external adamantane at 1.63 ppm as a secondary reference.

For these NMR experiments, the samples were synthesized as described above. All <sup>1</sup>H NMR experiments were conducted on a Bruker Avance DRX 400 NMR spectrometer operating at <sup>1</sup>H frequency of 400.31 MHz equipped with 5 mm inverse two-channel probe head with z-gradients. The single pulse excitation experiments were recorded using a 30° pulse angle with a recycle delay of 1 s averaging 32 scans. Stimulated echo sequence with bipolar gradient pulses and a longitudinal eddy current delay was used for the <sup>1</sup>H diffusion ordered spectroscopy (DOSY) experiments. The gradient strength was incremented in 16 steps from 2% to 95% of the maximum gradient strength. The diffusion time and the gradient pulse length were 100 ms and 2.0 ms with 2 s recycle delay, respectively. After Fourier transformation and baseline correction, the diffusion dimension of the 2D DOSY spectra was processed using the Bruker Topspin 1.3 software package. The diffusion analysis was performed using the Topspin T<sub>1</sub>/T<sub>2</sub> relaxation package.

X-ray diffractograms were recorded with a STOE Stadi P equipped with a Mythen 1k detector using monochromatized MoKα radiation. The sample was attached to polyvinyl acetate films with perfluoroether (Fomblin Y, Aldrich). The sample was measured in transmission in 0.015° steps (continuous scan, 150 s<sup>-1</sup>) covering a 2θ range from 1.5° to 43°. Rietveld refinement<sup>[49]</sup> was performed with Topas Academic v6 using the fundamental parameters approach,<sup>[50]</sup> based on a structural model for bassanite by Ballirano et al.<sup>[51]</sup> Crystalline phases were identified according to the PDF-2 database<sup>[52]</sup> using Bruker AXS EVA.<sup>[53]</sup>

TGA measurements were carried out on a Netzsch STA 409 PC LXXX in the temperature range from 30 to 400 °C using heating rates of 10 K min<sup>-1</sup> under air.

Laser microscopy images were taken with a Keyence VK 8710 with a wavelength of 658 nm.

## Supporting Information

Supporting Information is available from the Wiley Online Library or from the author.

## Acknowledgements

The microscopy equipment is operated by the electron microscopy center, Mainz, (EMZM) supported by the Johannes Gutenberg University. The authors thank Prof. H. Frey for access to the IR spectrometer and Prof. A. Möller for access to the X-ray powder diffractometer.

Open access funding enabled and organized by Projekt DEAL.

## Conflict of Interest

The authors declare no conflict of interest.

## Author Contributions

M.M. and T.H. carried out the experiments, M.M. and W.T. conceived the experiments, M.M., Z.D., M.K., M.M. and K.P. contributed to methods, M-M wrote the manuscript with contributions of M.M., Z.D., M.K. and W.T.

## Data Availability Statement

The data that support the findings of this study are available in the supplementary material of this article.

## Keywords

ball-milling, bassanite, calcium sulfate, nanoparticles, polymorphism

Received: November 20, 2021

Revised: January 21, 2022

Published online: February 6, 2022

- [1] J. E. Kogel, *Industrial Minerals & Rocks: Commodities, Markets, and Uses*, Society for Mining, Metallurgy, and Exploration, Littleton **2006**.
- [2] L. Pelletier-Chaignat, F. Winnefeld, B. Lothenbach, G. L. Saout, C. J. Müller, C. Famy, *Cem. Concr. Compos.* **2011**, *33*, 551.
- [3] J. Bizzozero, C. Gosselin, K. L. Scrivener, *Cem. Concr. Res.* **2014**, *56*, 190.
- [4] A. D. Ledingham, J. D. English, S. Akyalcin, B. E. Cozad, J. C. Ontiveros, F. K. Kasper, *Am J Orthod Dentofacial Orthop* **2016**, *150*, 1056.
- [5] Z. Zhou, F. Buchanan, C. Mitchell, N. Dunne, *Mater. Sci. Eng., C* **2014**, *38*, 1.
- [6] M. Younes, G. Aquilina, L. Castle, K.-H. Engel, P. Fowler, P. Fürst, R. Gürtler, U. Gundert-Remy, T. Husøy, W. Mennes, P. Moldeus, A. Oskarsson, R. Shah, I. Waalkens-Berendsen, D. Wölffe, P. Boon, R. Crebelli, A. Di Domenico, M. Filipic, A. Mortensen, H. Van Loveren, R. Woutersen, A. Giarola, F. Lodi, F. Riolo, M. J. Frutos Fernandez, *EFSA J.* **2019**, *17*, 5868.
- [7] M. V. Thomas, D. A. Puleo, *J. Biomed. Mater. Res., Part B* **2009**, *88*, 597.
- [8] N. Sindhura Reddy, S. Sowmya, J. D. Bumgardner, K. P. Chennazhi, R. Biswas, R. Jayakumar, *Biochim. Biophys. Acta* **2014**, *1840*, 2080.
- [9] G. Orsini, J. Ricci, A. Scarano, G. Pecora, G. Petrone, G. Iezzi, A. Piattelli, *J. Biomed. Mater. Res., Part B* **2004**, *68*, 199.
- [10] S. J. McConoughey, R. P. Howlin, J. Wiseman, P. Stoodley, J. H. Calhoun, *J. Biomed. Mater. Res., Part B* **2015**, *103*, 870.
- [11] J. Bensted, S. Prakash, *Nature* **1968**, *219*, 60.
- [12] B. Guan, G. Jiang, Z. Wu, J. Mao, B. Kong, *J. Am. Ceram. Soc.* **2011**, *94*, 3261.
- [13] H. Weiss, M. F. Bräu, *Angew. Chem., Int. Ed.* **2009**, *48*, 3520.
- [14] J. W. Anthony, *Handbook of Mineralogy*, Vol. 5, Mineral Data Publishing, Tucson **2003**.
- [15] A. Becker, I. Sötje, C. Paulmann, F. Beckmann, T. Donath, R. Boese, O. Prymak, H. Tiemann, M. Epple, *Dalton Trans.* **2005**, 1545.
- [16] A. E. S. Van Driessche, T. Stawski, M. Kellermeier, *Chem. Geol.* **2019**, *530*, 119274.
- [17] D. Freyer, W. Voigt, *Monatsh. Chem.* **2003**, *134*, 693.
- [18] M. Ossorio, A. E. S. van Driessche, P. Pérez, J. M. García-Ruiz, *Chem. Geol.* **2014**, *386*, 16.
- [19] a) J. K. Warren, *Evaporites: Sedimentology, Resources and Hydrocarbon*, Springer, Berlin **2006**. b) G. Testa, S. Lugli, *Sediment. Geol.* **2000**, *130*, 249.
- [20] F. Mees, M. De Dapper, *Sediment. Geol.* **2005**, *181*, 225.
- [21] Y. Langevin, F. Poulet, J.-P. Bibring, B. Schmitt, S. Douté, B. Gondet, *Science* **2005**, *307*, 1581.
- [22] F. Wirsching, in *Ullmanns Encyclopedia of Industrial Chemistry*, 7th ed., Wiley-VCH **2007**, p. 3824.
- [23] N. B. Singh, B. Middendorf, *Prog. Cryst. Growth Charact. Mater.* **2007**, *53*, 57.
- [24] H. Tiemann, I. Sötje, G. Jarms, C. Paulmann, M. Epple, B. Hesse, *J. Chem. Soc., Dalton Trans.* **2002**, *7*, 1266.
- [25] A. Saha, J. Lee, S. M. Pancera, M. Bräu, A. Kempter, A. Tripathi, A. Bose, *Langmuir* **2012**, *28*, 11182.
- [26] Y.-W. Wang, Y.-Y. Kim, H. K. Christenson, F. C. Meldrum, *Chem. Commun.* **2012**, *48*, 504.
- [27] F. Jones, *CrystEngComm* **2012**, *14*, 8374.
- [28] A. E. S. Van Driessche, L. G. Benning, J. D. Rodriguez-Blanco, M. Ossorio, P. Bots, J. M. García-Ruiz, *Science* **2012**, *336*, 69.
- [29] Y.-W. Wang, F. C. Meldrum, *J. Mater. Chem.* **2012**, *22*, 22055.
- [30] U. Tritschler, A. E. S. Van Driessche, A. Kempter, M. Kellermeier, H. Cölfen, *Angew. Chem., Int. Ed.* **2015**, *54*, 4083.
- [31] U. Tritschler, M. Kellermeier, C. Debus, A. Kempter, H. Cölfen, *CrystEngComm* **2015**, *17*, 3772.
- [32] T. M. Stawski, A. E. S. van Driessche, M. Ossorio, J. D. Rodriguez-Blanco, R. Besselink, L. G. Benning, *Nat. Commun.* **2016**, *7*, 11177.
- [33] C. Yan, J. Nishida, R. Yuan, M. D. Fayer, *J. Am. Chem. Soc.* **2016**, *138*, 9694.
- [34] K. He, A. Nie, Y. Yuan, S. M. Ghodsi, B. Song, E. Firlar, J. Lu, Y.-P. Lu, T. Shokuhfar, C. M. Megaridis, R. Shahbazian-Yassar, *ACS Appl. Nano Mater.* **2018**, *1*, 5430.
- [35] T. M. Stawski, A. E. S. Van Driessche, R. Besselink, E. H. Byrne, P. Raiteri, J. D. Gale, L. G. Benning, *J. Phys. Chem. C* **2019**, *123*, 23151.
- [36] T. M. Stawski, H. M. Freeman, A. E. S. Van Driessche, J. Hövelmann, R. Besselink, R. Wirth, L. G. Benning, *Cryst. Growth Des.* **2019**, *19*, 3714.
- [37] C. Jia, L. Wu, J. L. Fultron, X. Liang, J. J. De Yoreo, B. Guan, *CrystEngComm* **2020**, *22*, 6805.
- [38] C. Anduix-Canto, M. A. Levenstein, Y.-Y. Kim, J. R. A. Godinho, A. N. Kulak, C. González Niño, P. J. Withers, J. P. Wright, N. Kapur, H. K. Christenson, F. C. Meldrum, *Adv. Funct. Mater.* **2021**, *2107312*.
- [39] J. I. Escavy, M. J. Herrero, *Ore Geol. Rev.* **2013**, *53*, 504.
- [40] A. López-Delgado, S. López-Andrés, I. Padilla, M. Alvarez, R. Galindo, A. J. Vázquez, *Geomaterials* **2014**, *4*, 82.
- [41] M. Tang, X. Li, Y. Shen, X. Shen, *J. Appl. Crystallogr.* **2015**, *48*, 827.
- [42] P. Balaz, M. Achimovicoa, M. Balaz, K. Chen, O. Dobrozhan, E. Guilmeau, J. Hejtmanek, K. Knizek, L. Kubickova, P. Levisnky, V. Puchy, M. J. Reece, P. Varga, R. Zhang, *ACS Sustainable Chem. Eng.* **2021**, *9*, 2003.
- [43] S. Fukugaichi, N. Matsue, *ACS Omega* **2018**, *3*, 2820.
- [44] S. Leukel, M. Panthöfer, W. Schärtl, M. Mondeshki, W. Tremel, *Langmuir* **2018**, *34*, 7096.
- [45] D. R. G. Mitchell, B. Schaffer, *Ultramicroscopy* **2005**, *103*, 319.
- [46] Y. Sheng, M. Regner, *J. Phys. Chem. A* **2019**, *123*, 3334.
- [47] Eurogypsum, <https://www.eurogypsum.org/the-gypsum-industry/use-of-gypsum-in-buildings/> (accessed: October 2021).
- [48] Umweltbundesamt homepage, [www.umweltbundesamt.at](http://www.umweltbundesamt.at) (accessed: October 2021).
- [49] H. M. Rietveld, *J. Appl. Crystallogr.* **1969**, *2*, 65.
- [50] A. A. Coelho, *J. Appl. Crystallogr.* **2018**, *51*, 210.
- [51] P. Ballirano, A. Maras, S. Meloni, R. Caminit, A. Kirfel, G. Will, *Eur. J. Mineral.* **2001**, *13*, 985.
- [52] PDF-2, Release 2004, JCPDS – International Center for Diffraction Data, Newton Square, PA, USA **2004**.
- [53] EVA 10.0 Rev. 1, Bruker AXS, Madison, WI, USA **2003**.